Materials Advances

ROYAL SOCIETY OF CHEMISTRY

PAPER

View Article Online
View Journal | View Issue

Cite this: *Mater. Adv.*, 2025, **6**, 7114

Cost-effective carbon foam/paraffin composites for enhanced multifunctional energy conversion and storage

Arya Rahmani,[a] Ali Mohseni Ahangar,[a] Mahdi Maleki,*[a] Rouhollah Ahmadi[b] and Ahmad Shokrieh[c]

Phase change material (PCM) composites have been introduced in various application fields to optimize the balance between energy supply and consumption using renewable energy sources. However, intrinsic weaknesses of PCMs hinder their applications in industrial and residential applications. Herein, the high-strength, lightweight, highly thermally conductive, and cost-effective carbon foam (CF) was utilized as an encapsulation framework for a commercial PCM, paraffin wax (PW), *via* vacuum infiltration to overcome the limitations of PCMs. The prepared high-performance, shape-stabilized PCM composite is suitable for utilization in multiple applications, including solar thermoelectric power generators (TEGs), resistant heaters, and solar-to-heat converters. The prepared composite was installed on a water-cooled TEG to convert the light to electrical energy. When the proposed thermoelectric conversion system was irradiated with light intensities of 1700, 1800, and 1900 W m^{-2}, the output voltages were 0.63, 0.83, and 1 V, respectively. The capability of the PCM composite as a resistance heater in energy management of residential buildings at energy peak time was investigated by applying a voltage in the test room. After seven heating/cooling cycles between 55 and 60 °C by turning on/off the voltage under a constant power of 6 W, the temperature of the test room reached comfort conditions. After completely turning off the electrical heater, the release of latent heat energy contributed to maintaining the indoor temperature under convenient conditions. Such excellent performance revealed that the prepared low-cost CF possesses high potential for application in residential heating systems. Furthermore, the high light absorption capacity of commercial CF/PW enables efficient performance in the solar to thermal conversion process.

Received 13th May 2025,
Accepted 20th August 2025

DOI: 10.1039/d5ma00482a

rsc.li/materials-advances

1. Introduction

The growing global population and accelerating industrial activity have significantly increased energy demand, mounting pressure on conventional energy systems—particularly in light of the finite nature of fossil fuel resources.[1,2] An appealing method to respond to the imbalance between energy supply and consumption is the advancement of energy storage technologies—specifically, PCMs, which offer efficient thermal energy storage through latent heat absorption and release during phase transitions.[3,4] PCMs store thermal energy by absorbing latent heat during the solid-to-liquid phase transition and release it upon cooling within a narrow temperature range, which provides high storage density and effective temperature control.[5–8]

Among the available PCMs, paraffin-based materials are widely utilized due to their high latent heat capacity, moderate and stable melting point, good chemical and thermal stability, negligible supercooling, and non-corrosive and non-toxic nature.[9–13] However, their practical application is restricted by major disadvantages, which are leakage during phase change, and poor thermal and electrical conductivity which restrict their application in active energy conversion systems, particularly where light-to-heat or electrical-to-heat conversion is desired.[14–19]

In order to mitigate these disadvantages, incorporating PCMs within porous three-dimensional (3D) scaffolds is a feasible option to improve thermal conductivity, mechanical stability and structural stability.[20,21] Carbon-based materials, such as CF and graphene foam, have been proven to be especially effective due to their interconnected porosity, high

[a] *School of Metallurgy & Materials Engineering, Iran University of Science and Technology (IUST), Narmak, Tehran 16846, Iran. E-mail: malekim@iust.ac.ir; Tel: +982177459151*
[b] *School of New Technologies, Iran University of Science and Technology (IUST), Narmak, Tehran 16846, Iran*
[c] *Hoffmann Institute of Advanced Materials, Shenzhen Polytechnic University, 7098 Liuxian Boulevard, Shenzhen, Guangdong 518055, P. R. China*

thermal conductivity, capillary retention forces, and photothermal/Joule-heating capabilities.[20,22–25] These frameworks not only mitigate leakage and enhance heat transport but also broaden utilization of PCMs to areas including solar energy harvesting, electronic cooling, industrial heat recovery, and thermal buffering in power systems.[26–29]

PCMs supported by carbon-based materials are employed to convert solar/electrical/magnetic energy to thermal energy, as well as adsorb and store wasted heat from electronic devices, vehicles, or machinery. These capabilities are suitable for applications in construction, industrial operations, electronic devices, and solar energy systems.[26–30] Exceptionally efficient conversion of solar-to-thermal energy and high thermal conductivity of black CF/PCM composites lend themselves for use as solar collectors in TEGs.[29,31–34] It has been reported that the performance of TEGs was enhanced by employment of PCMs as heating and cooling media.[35,36] Infiltrated PCMs in the graphene aerogel with a 3D porous structure led to PCM composites that led to generation of stable and continuous electric energy from TEGs during heating and cooling processes.[37] High-strength cross-linked graphene/cysteamine aerogel supported by two different PCMs was attached to the two sides of TEGs to achieve the Seebeck effect and pyroelectric effect. The power generator incorporating PCM composites generated electrical energy.[38] The highly graphitized magnetic CF was used to advance thermoelectric performance with 0.81 V output voltage under 2100 W m^{-2}.[39] A photo-thermoelectric system, consisting of a PCM photothermal layer (CF/polyethylene glycol), a TEG, and a cooling layer, can deliver an output voltage of approximately 50 mV under 1000 W m^{-2}.[40] A hierarchical carbon nanostructure was deposited *via* simple chemical vapor deposition (CVD) using the flame of a candle to generate a voltage under 1000 W m^{-2} solar irradiation. As a result, the carbon absorber, which was coated on the thermoelectric module, produced 130 mV.[41]

The use of electrically conductive CFs as PCM containers makes it possible to generate and store the heat energy from electric energy. Based on heat generation ability, CF/PCM composites have been employed in various application areas such as green electrical heaters for domestic applications.[42–44] The CF/PCM composite as an electrical heater and *in situ* thermal energy storage device for buildings revealed a promising performance. In addition, it could maintain the temperature of a test room above 18 °C for 41 min without electricity consumption in energy peak load time.[42]

It is important to note that the applications of all carbon-based material/PCM composites require a high-quality carbon matrix with a low-cost and facile production process with commercial and cost-effective raw materials. Additionally, they need to address the challenges associated with organic PCMs, such as leakage, low thermal/electrical conductivity, and light absorption. This research aims to access a low-cost CF that has interesting properties and can be used for diverse energy conversion applications. The presented foam as a support for PW resulted in a composite with high light-to-heat/electric energy and electric-to-heat energy performance. Utilization of the presented composite on top of a TEG led to the generation of a high voltage of 1 V due to the Seebeck effect. In addition, the PCM composite as a resistance heater could produce heat efficiently and maintain the indoor temperature at convenient conditions (21 °C).

2. Experimental

2.1. Materials

Commercial melamine foam (MF) were bought from a local supplier, while commercial PW and phenolic resin were obtained from Behran Oil Co and Resitan Co, respectively. Additionally, cetyltrimethylammonium bromide (CTAB) was provided by Merck Company. Ethanol solution was purchased from Visyan Co.

2.2. Synthesis of carbon foam (CF)

Initially, a solution was prepared by dissolving 21.7 g of phenolic resin and 1.08 g of CTAB in 50 cc of an ethanol/water mixture at a 70/30 volume ratio. The MF was then cut to the desired size and immersed in this solution. After successful infiltration, the coated MF was dried at 100 °C. It was subsequently placed in a tube furnace, where it was heated to 900 °C for 90 minutes, with a heating rate of 2.5 °C min^{-1}.

2.3. Preparation of PCM composites

The PCM composites were created using the vacuum impregnation technique. PW was heated in a beaker at 70 °C to melt it completely. The CF was then immersed in the melted PW and transferred to a vacuum drying oven (50 mbar) set at 70 °C for one hour. After this process, any excess PW on the surfaces of the composite was removed. Fig. S1 depicts the synthesis process of CF and PCM composites.

2.4. Material characterization

X-ray diffraction (D8 advance, Bruker Germany) patterns were recorded with Cu-Kα radiation (λ = 1.5418 Å) to study the phase analysis of the samples. Nitrogen absorption was measured using a Belsorb mini (MicrotracBEL Corp.) at 77 K. Before analysis, the samples experienced degassing at 150 °C under vacuum conditions. Raman spectra were acquired on a Horiba Xplora microscope system utilizing a 785 nm laser. Scanning electron microscopy (SEM, TESCAN VEGA//XMU microscope) and transmission electron microscopy (TEM, JEM-2100F) were employed to observe and characterize the morphology and microstructure of the samples, respectively. Fourier transform infrared (FTIR) spectra were recorded by using a Spectrum RX I (PerkinElmer). All spectra in the 400–4000 cm^{-1} range with a 4 cm^{-1} spectral resolution were obtained from compressed KBr pellets. KBr was thoroughly dried by heating it in an oven at 110–130 °C for several hours. Subsequently, a small amount of the sample (typically around 1–2 mg) was carefully cut and accurately weighed. This was then homogeneously mixed with approximately 100 mg of dry KBr powder, maintaining a common ratio of 1 : 100. The mixture was finely ground using

an agate or ceramic mortar and pestle until it became a uniform and fine powder. Then, the powder was compressed under high pressure using a hydraulic press to form a transparent pellet. Finally, the resulting pellet was placed in the sample holder of the FTIR spectrometer, and the spectrum was recorded. Differential scanning calorimetry (DSC) was conducted using a DSC (Q100, TA Instruments) under a nitrogen atmosphere, with a heating/cooling rate of 5 °C min^{-1}. The reliability of PCM composites was evaluated through 200 heating/cooling cycles. Each cycle involved heating the composites with dimensions of 10 mm × 10 mm × 10 mm above the melting point of the PCMs and cooling them below their freezing temperature. In the reliability test, the sample was placed on a hot plate (60 °C) for 1 min and then transferred to a cooled plate (room temperature) for 1 min. The rest time between the heating and cooling was 1 min. For practical tests, to measure the temperature of the composite, test room, and environment temperatures, the T-type thermocouples were utilized. To record the composite temperature, a thermocouple was embedded in the middle of the sample. A data acquisition device (midi logger GL840) was employed to record the temperature variations. The uncertainty of temperature and voltage in the midi logger GL840 is 0.1% of rdg +0.5 and 0.1% of F.S., respectively. Moreover, an infrared camera (UNI-T) was utilized to monitor the heat transfer of the samples when being placed on a hot plate that was kept at a constant temperature.

2.5. Test rooms

The energy-saving potential and thermal buffering performance of the PCM composite were evaluated using wooden test chambers with cubic dimensions of 50 × 50 × 50 cm, simulating small-scale indoor environments. To investigate the response of the composite to solar irradiation, it was irradiated using a xenon arc lamp under controlled light intensities. Temperature variations within the chamber were continuously monitored and recorded using a multi-channel temperature data logger.

To assess the thermoelectric performance of the composite, it was positioned on top of a commercial thermoelectric generator (TEG, model TEC1-12710). The dimensions of this TEG are 40 mm × 40 mm, and its operating voltage is 12 V, with a current of 10 A. A water-cooled heat sink system was placed beneath the TEG to ensure effective thermal management and maintain a stable temperature gradient across the device. The cooling system consisted of a circulating water bath coupled with an aluminum heat sink. The cooling system flow rate was 2 L min^{-1}. Two thermocouples were embedded at different depths within the PCM composite to measure the internal temperature gradient: one located in the upper third of the material (T1) and the other in the lower third (T2). A schematic illustration of the experimental setup is provided in Fig. S2.

To evaluate the performance of the composite as a resistive heater for potential peak-load energy management in buildings, additional experiments were conducted using miniature wooden test chambers with internal dimensions of 10 × 10 × 10 cm. The composite was electrically connected to a laboratory DC power supply *via* copper wires attached to opposing sides. Three thermocouples were employed to monitor temperature evolution: inside the test chamber (T-R), within the composite body (T-C), and in the surrounding environment (TE). The heating process was recorded using a temperature data acquisition system as the composite was energized to reach and maintain the thermal comfort range. The wooden test chamber is shown in Fig. S3.

3. Results and discussion

3.1. CF synthesis

Fig. 1a shows the XRD patterns of the prepared CF through pyrolysis of coated MF. Two broad shoulders are observed at approximately 23° and 43°, which are characteristic of a turbostratic carbon structure, indicating partial ordering and stacking disorder of graphene layers.[45] The Raman spectrum of CF in Fig. 1b displays two sharp peaks at around 1602 and1340 cm^{-1}. The former, the G band, was ascribed to the in-plane displacement of strongly bonded carbon in the hexagonal sheets. The latter corresponds to sp^3 carbon atom vibrations and indicates defect sites in the carbon structure (D-band).[46] The relative intensity ratio of the D-band to G-bands (I_D/I_G ratio) is proportional to the evolution of graphitized domains in the carbon microstructure.[47] In this regard, the I_D/I_G ratio can be examined. This ratio was calculated to be approximately 0.93 for the prepared CF. The relatively low I_D/I_G ratio of the samples shows the simultaneous presence of defect sites and well-defined graphitic domains.[48] Fig. 1c shows the N_2 sorption isotherm of the synthesized CF. The BET surface area and pore volume of the CF sample were 197 $m^2 g^{-1}$ and 0.083 $cm^3 g^{-1}$, respectively. The C 1s spectrum (Fig. 1d) of CF has been divided into four peaks, which are located at 284.78, 285.5, 286.4, and 287.4 eV, and can be attributed to C–C/C═C, C–N, C–N/C–O, and C═O, respectively.[49–52] The appearance of nitrogen bonds can be owing to the presence of nitrogen in the initial MF.

3.2. CF morphology

The carbonization process of the coated MF resulted in approximately 31% shrinkage in the final CF structure compared to the original MF volume, as illustrated in Fig. S4. SEM images of the resulting CF (Fig. 2a and b) reveal an interconnected porous network, confirming the successful formation of a three-dimensional open-cell structure. TEM images (Fig. 2c and d) further highlight the hierarchical porosity of the pyrolyzed CF. In addition to the larger framework pores, well-defined nanopores are visible, indicating a hierarchical porous architecture.

3.3. CF/PW composite characterization

The performance of CF as a conductive encapsulation matrix for PCMs is highly dependent on the complete and uniform infiltration of the PCM into its porous framework. As shown in the SEM images (Fig. 2e and f), PW was successfully impregnated into the interconnected structure of CF, indicating thorough pore filling. This structural integration is essential

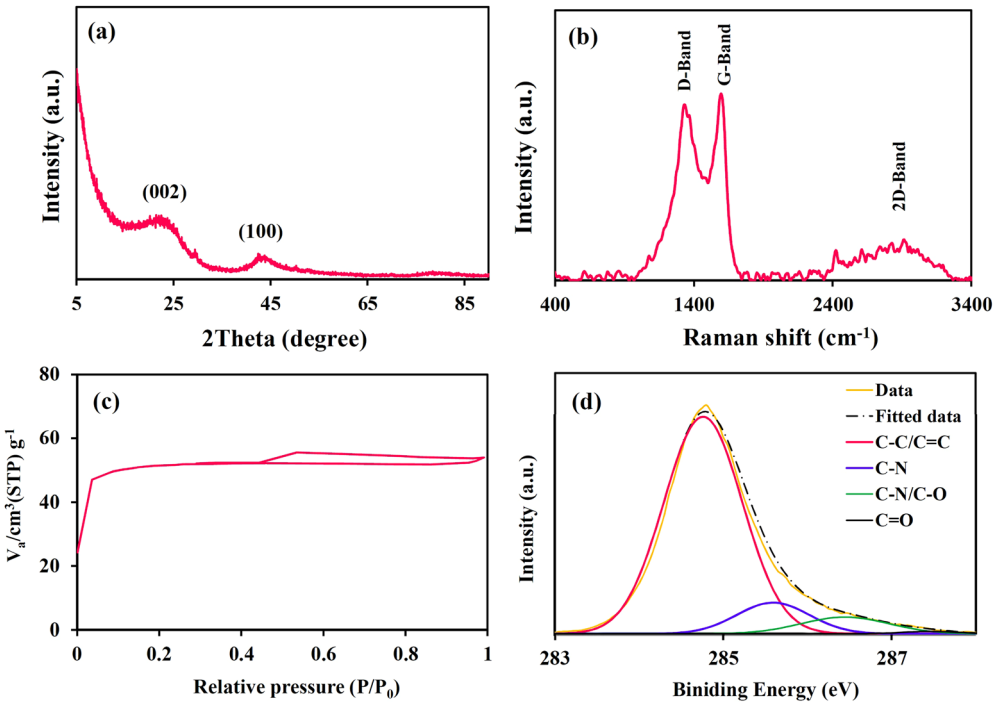

Fig. 1 (a) XRD pattern, (b) Raman spectrum, (c) BET diagram, and (d) XPS curve of the CF.

to ensure efficient thermal conduction and light-to-heat or electricity conversion in advanced energy storage and conversion systems.

DSC analysis was used to measure the phase change temperature and latent heat of the PW, CF/PW composite, and CF/PW composite after 200 frequent heating/cooling cycles (Fig. 3). Table 1 presents the detailed results of the DSC curves where T_m/T_c and $\Delta H_m/\Delta H_c$ are the peak melting/crystallization temperatures and enthalpies of the PW and PCM composite, respectively. Two primary minor and sharp endothermic peaks were detected in the DSC curves of PW and its composite during heating from 25° to 70 °C. The first peak can be attributed to solid–solid transformation. This transformation was attributed to the disordering of the monoclinic crystals to a pseudohexagonal crystal.[53] The sharp peak between 50 °C and 64 °C during heating was assigned to the solid–liquid phase change of PW. The required energy to melt the PW in this transition period is 112.7 J g^{-1}. The solidification cycle led to the start of crystallization at 57.3 °C and completed at 43 °C with a released energy of 108.9 J g^{-1}. Upon incorporation into the CF matrix, the melting and solidification transitions of PW occurred at slightly reduced temperatures, a typical effect of confinement within porous structures. The melting and crystallization enthalpies for the CF/PW composite were measured as 74.9 and 71.3 J g^{-1}, respectively, indicating effective energy storage. One way to evaluate the performance of CF/PW is to compare its latent heat to that of PW, which demonstrates the extent of PW infiltration into the CF. The latent heat of PW is 112.7 J g^{-1}, while the CF/PW has a latent heat of 74.9 J g^{-1}. The ratio of the latent heat of the CF/PW to that of PW is 66%.

To assess long-term thermal reliability, the composite was subjected to 200 consecutive heating/cooling cycles. The DSC curve of the composite after the cycling process demonstrated excellent thermal stability, with only minor reductions in melting and crystallization enthalpies (~9% decrease for both). Additionally, the degree of supercooling decreased slightly from 4.79 °C to 4.58 °C, confirming that the composite retained favorable phase change dynamics under extended operating conditions. These results validate the CF/PW composite as a durable and efficient thermal energy storage material for sustainable energy applications.

The XRD patterns of pure PW and the CF/PW composite are presented in Fig. 4a. The comparison reveals that the crystalline structure of PW remains largely intact upon confinement within the CF matrix, indicating that no significant degradation or phase transformation occurs during composite formation. Moreover, no additional diffraction peaks are observed, suggesting that no new crystalline phases are generated during the infiltration process. The displacement of 2θ in the XRD pattern is negligible after composite formation. The main peak of PW appeared at 21.4°, while the mentioned peak shifted to 21.2° for the composite. Notably, after the frequent cycling process, this peak has returned to 21.4°. Applying the Debye–Scherrer equation, the crystallite sizes of PW, the composite, and the composite after 200 cycles are determined to be 4.2 Å, 6.2 Å, and 6.56 Å. Nevertheless, the confinement of the PCM within the porous network of the CF led to modifications in the crystallographic planar growth compared to the pure PW. This behavior is consistent with prior studies reporting the preferential orientation of PCM crystals in confined porous matrices such

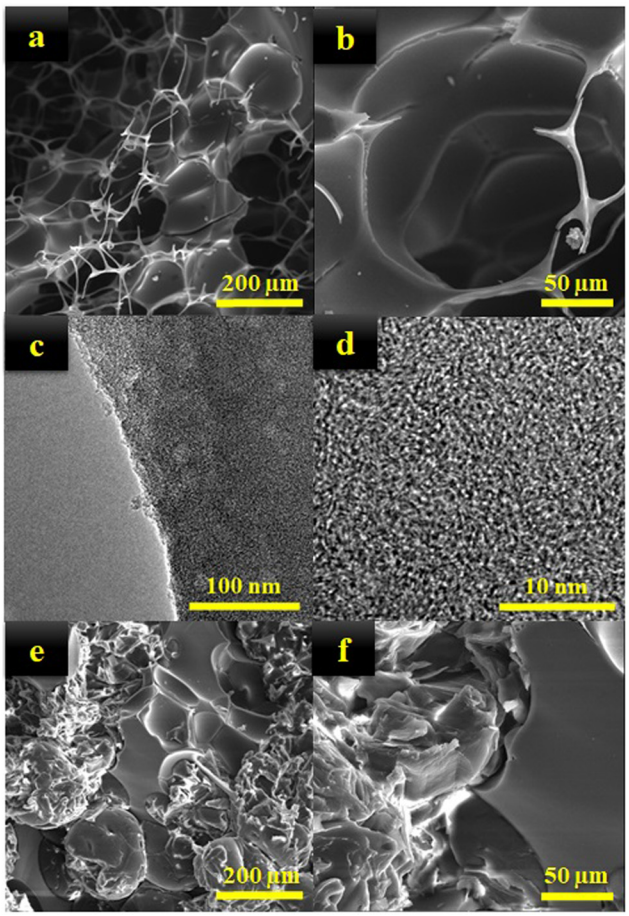

Fig. 2 (a) and (b) SEM images of the obtained CF at different magnifications, (c) and (d) TEM images of the porous structure of the synthesized CF, and (e) and (f) SEM images of the encapsulation of PCMs in the porous structure of the CF.

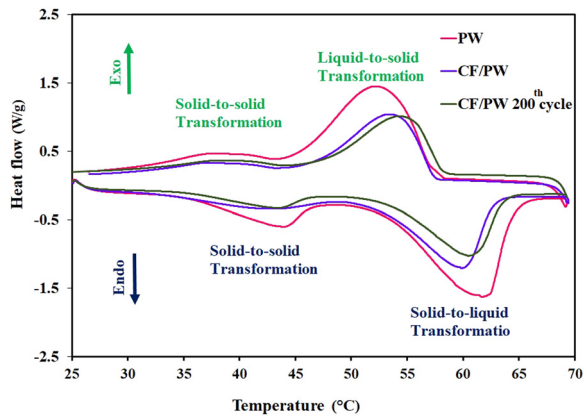

Fig. 3 DSC curves of PW, the CF/PW composite, and the composite after the 200th cycle of heating/cooling.

as graphene and graphene oxide aerogels, polyacrylonitrile (PAN)-derived CFs, and polystyrene–carbon nanotube (PS–CNT) polyHIPE foam. In such systems, the architecture of the

Table 1 DSC data of PW, the CF/PW composite, and the composite after the 200th cycle of heating/cooling

Sample	T_m (°C)	$T_{m,peak}$ (°C)	ΔH_m (J g^{-1})	T_c (°C)	$T_{c,peak}$ (°C)	ΔH_c (J g^{-1})	Supercooling (°C)
PW	53.1	61.7	112.7	57.3	52.6	108.9	4.2
CF/PW	52.6	59.8	74.9	57.4	53.7	71.3	4.8
CF/PW 200th cycle	53.6	60.5	67.5	58.2	54.6	64.6	4.6

porous scaffold plays a critical role in directing crystal nucleation and growth during the solidification process. Notably, two-dimensional materials like graphene oxide can serve as structural templates, guiding the alignment of PCM molecules and promoting the formation of ordered crystal domains with preferred orientations.[10,26,54]

To assess the chemical stability of PW after integration into the CF, FTIR spectroscopy was conducted for both pure PW and the CF/PW composite (Fig. 4b). Specifically, the asymmetric and symmetric C–H stretching bands, typically observed at 2920 cm^{-1} and 2850 cm^{-1}, are retained in the composite spectrum, confirming the preservation of the alkyl chain structure. Additionally, the bending vibrations of –CH_2 and –CH_3 groups, observed near 1466 cm^{-1}, remain unchanged, further supporting the physical nature of the interaction. The peak at

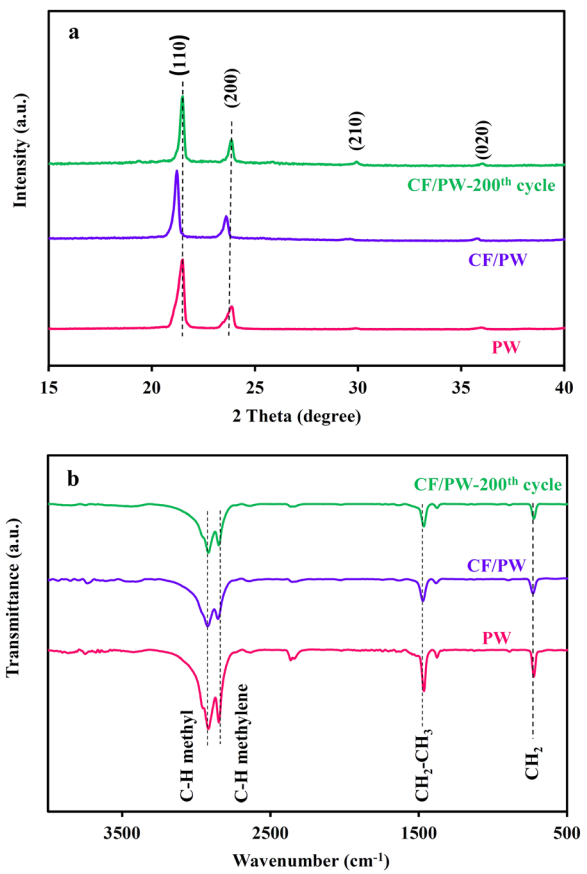

Fig. 4 (a) XRD patterns (b) FTIR spectra of PW and the CF/PW composite before and after thermal cycles.

730 cm^{-1}, corresponding to in-plane rocking vibrations of CH_2, is also present in both spectra without a significant shift. These results suggest that the formation of the CF/PW composite primarily involves physical encapsulation, with no evident chemical bonding or structural modification of the PW. The preservation of functional group positions and vibrational modes supports the conclusion that the CF acts as an inert, thermally conductive scaffold, enabling stable PCM confinement while maintaining its phase change properties.[54–56] To further investigate thermal durability, the composite was subjected to 200 consecutive heating and cooling cycles. As shown in Fig. 4a and b, the XRD and FTIR spectra of the composite after cycling reveal no significant changes in either crystal structure or chemical composition. The absence of new peaks or shifts in both spectra indicates that repeated melting and solidification of the encapsulated PW do not compromise its structural or chemical stability. Moreover, the calculated crystallite size of PW remains nearly unchanged after 200 phase transition cycles, confirming that the composite retains its crystalline nature and is not degraded by thermal cycling. These results demonstrate excellent thermal reliability and long-term stability of the CF/PW composite, a key requirement for its deployment in practical energy storage applications.

3.4. Thermal response and heat transfer behavior

To evaluate the effect of the thermal conductive network of the CF on the heat transfer rate of the prepared composite, the temperature response of the composite to temperature variation was recorded using an IR camera (Fig. 5a). Both pure PW and the CF/PW composite were placed on an isothermal hot plate, and their thermal responses were recorded over time. Although the temperatures of both materials increased continuously, the CF/PW composite exhibited a noticeably faster temperature rise compared to pure PW under identical conditions. This enhanced thermal response became even more pronounced over extended exposure, indicating superior heat transfer efficiency in the composite structure. During the cooling process, the composite also demonstrated a more rapid temperature drop than pure PW. This improved thermal behavior was attributed to the presence of a three-dimensional interconnected porous carbon network, which promotes efficient heat conduction through the pore walls. The porous structure resulted in the formation of small PW domains surrounded by carbon pore walls. These smaller domains, being in close contact with the conductive carbon framework, facilitated effective heat transfer from the carbon walls to the insulating PW phase. The ability of these networks to accelerate both heat absorption and release underscores the suitability of the CF/PW composite for applications that demand fast and reliable thermal energy management. Similar effects have been reported in PCM systems incorporating thermally conductive porous matrices such as graphene aerogels, graphitic foam, and other carbon-based scaffolds.[57–59] To quantitatively observe this phenomenon, both PW and the CF/PW were placed on a hot plate and heated to 51 °C. A thermocouple was inserted into each sample to monitor the temperature increase. Fig. S5 shows temperature–time curves of the CF/PW composite and PW on a hot plate.

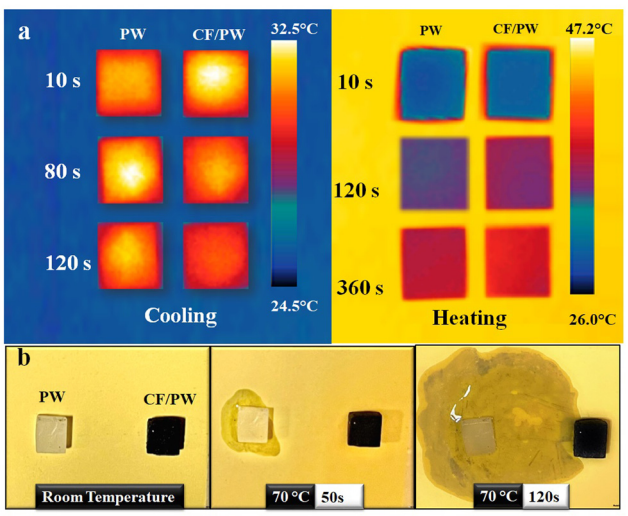

Fig. 5 (a) Heat transfer rate of PW and the CF/PW composite during heating and cooling, and (b) leakage test performance of the pure PW and the CF/PW composite at 70 °C.

3.5. Dimensional stability and leakage resistance

The dimensional stability and leakage resistance of the CF/PW composite were evaluated to examine the effectiveness of the CF in physically confining the PCM within its porous network during the melting process. Both pure PW and the CF/PW composite were placed on a hot plate and subjected to controlled heating. At temperatures of 60 °C and 70 °C, visual observations were recorded to assess structural integrity over time (Fig. 5b). Under these conditions, pure PW began to melt visibly after 90 s at 60 °C and after just 15 s at 70 °C, leading to progressive leakage and spreading across the surface of the hot plate. In contrast, the CF/PW composite maintained its original shape and exhibited no leakage over the same time intervals, even under the higher temperature. After 120 s at 70 °C, pure PW had fully liquefied and spread extensively, while the composite remained structurally stable with no observable liquid exudation. The amount of PW leakage from the CF/PW after 50 s and 120 s was 0 and 0–1 wt%. This improved dimensional stability is attributed to the highly porous and interconnected structure of the CF, which acts as a physical barrier that traps the PCM within its internal network. The strong capillary forces and surface tension within the CF pores help retain the molten PCM, effectively preventing leakage. Additionally, physical interactions between the CF matrix and the PW molecules further enhance shape stability. The encapsulating framework functions as a structural shell that restricts PCM mobility during phase transition, ensuring leakage resistance and improving the practical applicability of the composite in thermal energy storage systems.[60–62]

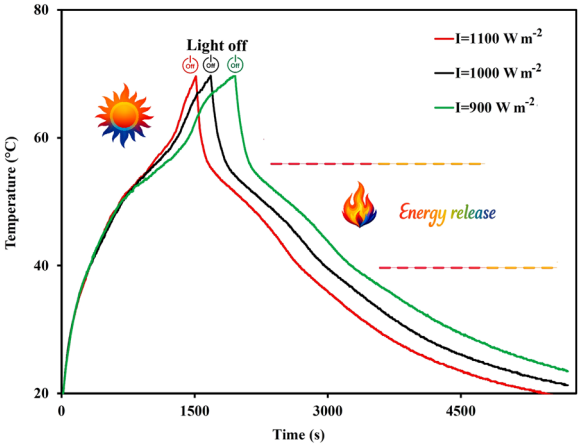

Fig. 6 Temperature–time curves of the CF/PW composite during solar to thermal energy conversion.

3.6. Solar-to-thermal energy conversion

The incident light-to-thermal energy conversion performance of the CF/PW composite was evaluated under simulated solar irradiation at fixed intensities of 900, 1000, and 1100 W m^{-2} (Fig. 6). Under illumination at 900 W m^{-2}, the surface temperature of the composite increased steadily, reaching 50 °C after 673 s. At this point, the onset of melting was observed, as evidenced by a noticeable reduction in the slope of the temperature–time curve. The melting process proceeded over the next 883 s, during which the latent heat was absorbed. Following the completion of melting, the temperature of the composite increased rapidly, reaching approximately 70 °C under continued irradiation. When the light source was switched off, the temperature of the composite dropped quickly to 58 °C, followed by the appearance of a plateau region. This plateau corresponds to the solidification phase transition, during which the stored latent heat was released. The distinct inflection points and reduced slope regions present in the temperature profile indicate phase change behavior and energy release during solidification.[63]

The efficiency (η) of light-to-thermal storage of the fabricated CF/PW can be determined according to the ratio of the heat stored in the composite concerning the irradiated light energy absorbed during the phase change period. The following equation can be used to calculate the thermal storage efficiency:[64]

$$\eta = \frac{m \times \Delta H_c}{\rho \times S \times (t_f - t_s)} \quad (1)$$

where m corresponds to the mass of the composite, ΔH_c represents the phase change enthalpy measured by DSC, ρ is the incident light intensity of the simulated light source, S denotes the surface area of the sample, and t_f and t_s refer to the duration of the light-driven phase change before and after the phase change, respectively. According to eqn (1), the thermal energy storage efficiency (η) of the CF/PW composite was calculated to be approximately 71% under a light irradiation intensity of 900 W m^{-2}. This high efficiency at low light intensity is attributed to the strong light absorption of the black CF, the substantial infiltration of PW within its porous structure, and the high specific heat capacity of the composite. These factors work synergistically to enhance photothermal conversion and latent heat storage. The observed efficiency demonstrates that CF-based PCM composites perform competitively with a variety of advanced systems, including CFs, aerogels, and other additive-enhanced PCMs reported in the literature.[65–67] The incorporation of organic PCMs (1-hexadecanamine and palmitic acid) into the biomass carbon aerogels revealed a light-to-thermal conversion efficiency of 75.6%.[68] The composite of PW and CF, obtained through the high-temperature carbonization of resorcinol–formaldehyde resin and loofah sponge, resulted in a high photothermal energy conversion efficiency that reached up to ~84% under 1000 W m^{-2}.[69]

3.7. Thermoelectric application

To evaluate the influence of the CF/PW composite on the thermoelectric energy conversion performance, a test system comprising the CF/PW composite, a commercial TEG, a heat sink, and a water cooling loop was assembled and exposed to simulated solar irradiation at intensities of 1700, 1800, and 1900 W m^{-2}. The corresponding temperature–time curves under different light intensities are presented in Fig. 7a. Under an irradiation intensity of 1700 W m^{-2}, the surface (T1-1700) and internal (T2-1700) temperatures of the composite rose steadily to 68.8 °C and 32.4 °C, respectively, within 1344 s.

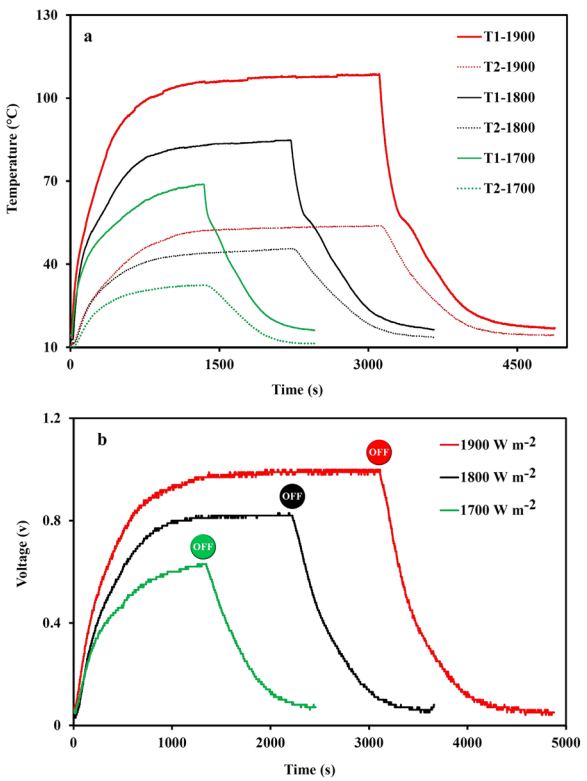

Fig. 7 (a) Temperature–time curves, and (b) open-circuit voltage of the thermoelectric conversion system with the CF/PW composite under the light intensities of 1700, 1800 and 1900 W m^{-2}, respectively.

Upon termination of the light source, a sharp temperature drop was observed in the T1-1700 profile. When T1-1700 reached approximately 58 °C, a distinct temperature plateau appeared, signifying the onset of phase change as PW began to solidify. In contrast, the internal temperature (T2-1700) exhibited a slower decline, which can be attributed to the latent heat release from the gradual solidification of PW in the inner layers. This behaviour confirms the effective thermal buffering capability of the composite during phase transition. The open-circuit voltage output measured during the experiment is shown in Fig. 7b. Under 1700 W m^{-2}, the voltage increased steadily and reached 0.63 V at 1344 s. As the temperature rise plateaued, the light source was turned off, and a delayed voltage drop followed. This gradual decline in voltage is a result of the heat retention and release properties of the PW, which continued to supply thermal energy to the TEG even after irradiation ceased.

A similar temperature–voltage response was observed under higher light intensities of 1800 and 1900 W m^{-2}, with correspondingly greater temperature gradients and voltage outputs. At a constant exposure time of 1344 s, the surface temperatures T1-1800 and T1-1900 reached 83 °C and 106 °C, respectively, both significantly higher than the 68.8 °C observed under 1700 W m^{-2}. Notably, beyond this point, the temperature profiles of the CF/PW composite at both higher intensities exhibited plateau regions, indicating sustained phase change until the light source was turned off. The open-circuit voltages measured under 1800 and 1900 W m^{-2} were 0.83 V and 1.00 V, respectively, as shown in Fig. 7b. This 1.00 V output represents one of the highest reported open-circuit voltages for TEGs integrated with PCM-based photothermal systems. For comparison, a top-down hierarchical structure consisting of an infiltrated CF with PEG as a photothermal layer, a TEG, and a hydrophilic CF layer as a cooling layer under light irradiation resulted in an open-circuit voltage of about 0.50 mV.[40] The open-circuit voltages of the MF@polypyrole-polymerized octadecylsiloxane/graphene nanoparticles/PW composite were reported to be 0.78 and 0.91 V at 2000 and 4000 W m^{-2}, respectively.[6] The 3D xerogel foam installed on the TEG have been employed for both self-floating water evaporation and thermoelectric power generation purposes. When the presented set-up was irradiated with light intensity of 1000, 2000, and 3000 W m^{-2}, the output voltage gradually increased from 0.14 V to 0.2 V and 0.24 V, respectively.[70] The TEG, heat sink, and hybrid nanocomposite containing RT54HC PCM and graphene-silver nanoparticles were employed to produce voltage. The melted nanocomposite was placed on the hot side of the TEG using an aluminum foil cup after reaching a temperature of 68 °C. Moreover, the cold side of the thermoelectric generator is appropriately attached to a heat sink. The setup produced a voltage of 425 mV.[71] A phase-change composite consisting of a carbonized polyimide/Kevlar nanofiber, $CoFe_2O_4$ nanoparticles, polyethylene glycol, and polypyrrole was used on the hot side of the thermoelectric generation system. The cold side was immersed in air and ice water. Under 2000 k m^{-2} solar irradiation, the developed setup in ice water showed a maximum output voltage of 259.7 mV.[72] Moreover, the voltage–temperature curves under different light intensities are presented in Fig. S6.

3.8. Electric-to-thermal energy conversion and storage

To evaluate the energy management potential of the synthesized composites, they were employed as resistive heaters to simulate peak-load regulation in residential building environments. During testing, a direct voltage was applied to the composite, and the resulting surface temperature and indoor ambient temperature were monitored simultaneously. A constant electrical power of 6 W was supplied by applying 3 V across the composite, enabling *in situ* conversion of electrical energy into thermal energy. This configuration allowed for the evaluation of both energy storage and heat delivery performance of the composite under controlled conditions, providing valuable insights into its practical applicability for reducing peak electricity demand in smart building systems.

In the first experimental scenario, the CF/PW composite was evaluated as a resistive heater to increase the ambient temperature of a small test chamber to a thermally comfortable range. To achieve this, a series of controlled on/off heating cycles were performed, alternating between 55 °C and 70 °C. The resulting heating curves under constant power input are illustrated in Fig. 8. In this figure, T70-C and T70-R correspond to the temperatures of the composite surface and the test room, respectively. During the first cycle, the composite temperature increased steadily from 8.3 to 70 °C over a period of 974 s, while the room temperature simultaneously rose to 16.3 °C. Upon reaching 70 °C, electrical input was interrupted, causing the composite to cool to 55 °C before initiating the next cycle. In the second cycle, heating from 55 °C to 70 °C required only 510 s, during which the room temperature increased to 17.9 °C. Subsequent heating cycles further elevated indoor conditions, with room temperatures reaching 18.6 and 20.2 °C at the end of the third and fourth cycles, respectively.

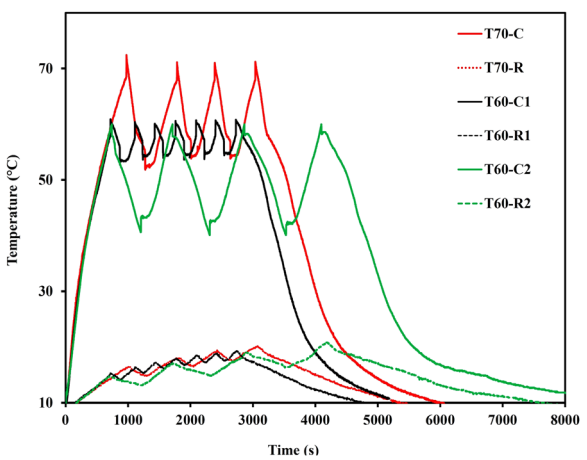

Fig. 8 Temperature–time curves of the CF/PW composite during the electric–thermal conversion process when the turn on/off of the electricity was applied in three temperature thresholds of 55–70, 55–60 and 40–60 °C.

Table 2 Details of consumed electrical energy to increase the temperature of the test room[a]

Temperature	Power (W)	Time based on maximum temperature of T60-R1 (19.4 °C)	Power × time (W s)
T70-C	6	2390	14 340 ± 3%
T60-C1	6	2745	16 470 ± 3%
T60-C2	6	4010	24 060 ± 3%

[a] Time based on the maximum temperature of T60-R1 (19.4 °C).

Following complete power shutdown, the composite began to cool, and the T70-C curve exhibited a noticeable change in the slope around 58 °C, indicating latent heat release due to the phase change of PW. In contrast, the room temperature (T70-R) decreased gradually and remained above 15 °C for over 900 s, confirming the effective thermal buffering provided by the PCM during solidification.

To further investigate how temperature thresholds affect room heating performance, the CF/PW composite heater was tested using two additional heating and cooling ranges, which were 55–60 °C and 40–60 °C. When the threshold range of 55–60 °C was selected, the composite surface temperature (T60-C1) reached 60 °C in a shorter duration of 740 s. However, due to the reduced maximum temperature, more cycles were required to elevate the room temperature to a comfortable level. In this configuration, the system underwent seven heating/cooling cycles, and the corresponding room temperatures (T60-R1) recorded at the end of each cycle were 15.3 °C, 16.2 °C, 17.8 °C, 18.4 °C, 18.8 °C, and 19.4 °C, respectively.

When a broader threshold of 40–60 °C was applied, a noticeable delay occurred in the second heating cycle, as full crystallization of the PCM took place during the extended power-off period. This condition influenced the thermal response of the composite (T60-C2). In this case, only four heating/cooling cycles were required to achieve a room temperature above 19.4 °C. Additionally, as the room temperature increased, the duration of each subsequent heating cycle decreased due to reduced thermal gradients and enhanced retention of heat within the environment. Details of the consumed electrical energy at the same room temperature (19.4 °C) for different temperature thresholds of heater are shown in Table 2. The required time for every heating/cooling cycle of the composite decreased when the room temperature increased. As noticed, different 3D carbon materials such as CNTs, the graphene aerogel, and graphite foam have been utilized as electrical/conductive frameworks for PCMs for electro-to-thermal energy conversion.[31,73–75] Notably, most energy conversion processes reported in the literature have been conducted under thermally isolated conditions and with small-sized composite samples. In contrast, the present study demonstrates the application of the CF/PW composite in increasing the temperature of the surrounding environment, highlighting its practical utility in open systems. To gain a more precise understanding of the intrinsic energy conversion efficiency, a thermally isolated composite sample with dimensions of 10 mm × 10 mm × 3 mm was subjected to a constant voltage. The resulting temperature response is illustrated in Fig. S7. In previous work, MF incorporated with reduced graphene oxide, graphene nanoplatelets, and PW exhibited an electro-thermal conversion efficiency of approximately 62.5% under a 2.9 V bias.[76] In the same study, a simple and cost-effective strategy was introduced by combining inorganic and organic functional materials with PCMs, obtaining a carbon cloth/PW/thermoplastic polyurethane (TPU)-coated composite that exhibited an electro-thermal conversion efficiency of up to 67.39% at 4.0 V.[77] While these systems performed well under thermally isolated conditions, the CF/PW composite developed in this study demonstrated excellent and tunable electro-thermal performance in a non-isolated environment, successfully heating the surrounding test room. In addition to its high heating efficiency, the composite also maintained excellent shape stability throughout operation, as shown in Fig. S8. These combined attributes suggest that the fabricated composite is a strong candidate for scalable applications in building energy management and other thermal regulation systems.

In summary, the prepared low-cost composite demonstrated excellent multifunctional performance. It produced a high open-circuit voltage of 1 V under a light intensity of 1900 W m^{-2} when used for a TEG, showed strong capability as an electrical heater, and exhibited efficient light-to-heat conversion. These features make it a promising material for future applications in energy storage and thermal management systems.

4. Conclusions

CF was successfully synthesized by pyrolyzing phenolic resin-coated commercial MF at 900 °C. The resulting structure was lightweight, mechanically robust, and highly porous, capable of accommodating a large quantity of PW. The CF/PW composite exhibited excellent shape stability and effectively prevented leakage during phase transition, making it a strong candidate for PCM encapsulation. The composite demonstrated strong solar-to-thermal energy conversion performance, achieving a light-to-thermal efficiency of 71% under a relatively low solar irradiance of 900 W m^{-2}. This high efficiency was attributed to its porous architecture and black surface, which enhanced photothermal absorption and energy retention. The efficient heat harvesting ability of the composite enabled its use as the thermal input for downstream energy conversion applications. Building on its photothermal performance, the composite was integrated into a thermoelectric energy harvesting setup, consisting of a PCM layer, a thermoelectric generator (TEG), a heat sink, and a water cooling loop. Upon exposure to solar irradiation at 1900 W m^{-2}, the system generated a high open-circuit voltage of 1 V. This output is among the highest reported values for TEG systems assisted by PCM layers, highlighting the effectiveness of the composite in bridging solar-thermal and thermoelectric energy conversion. In addition to solar-assisted power generation, the composite exhibited excellent performance as a low-cost electrical heater. Thanks to its high thermal storage capacity, electrical conductivity, and structural

integrity, it enabled efficient electro-to-thermal conversion. Under a constant power input of 6 W, the composite completed seven ON/OFF heating cycles between 55 °C and 60 °C, increasing the test room temperature to a comfortable level with a total energy input of 16 470 W s. The system also allowed programmable thermal cycling for energy-efficient indoor heating. Overall, the CF/PW composite offers a multifunctional platform for integrated solar harvesting, energy storage, thermoelectric generation, and low-power heating applications, making it a strong candidate for building-scale energy management solutions.

Author contributions

Arya Rahmani: writing – original draft, visualization, validation, methodology, investigation, formal analysis, data curation, and conceptualization. Ali Mohseni Ahangar: writing – original draft, visualization, validation, methodology, investigation, formal analysis, data curation, and conceptualization. Mahdi Maleki: writing – review and editing, writing – original draft, visualization, validation, supervision, methodology, investigation, and conceptualization. Rouhollah Ahmadi: visualization, validation, data curation, and conceptualization. Ahmad Shokrieh: review and editing, investigation, and conceptualization.

Conflicts of interest

The authors have disclosed that they have no conflicts of interest regarding the conduct of this study and the publication of its findings.

Data availability

All data supporting the findings of this study are available within the article and its Supplementary Information.

Supplementary information is available. See DOI: **https://doi.org/10.1039/d5ma00482a**.

References

1 Z. Tao, *et al.*, Phase change material based on polypyrrole/Fe3O4- functionalized hollow kapok fiber aerogel matrix for solar/magnetic- thermal energy conversion and storage, *Chem. Eng. J.*, 2021, **423**, 130180.
2 M. Maleki, *et al.*, Low-cost carbon foam as a practical support for organic phase change materials in thermal management, *Appl. Energy*, 2020, **258**, 114108.
3 X. Liu, *et al.*, Development of cost-effective PCM-carbon foam composites for thermal energy storage, *Energy Rep.*, 2022, **8**, 1696–1703.
4 Y. Li, *et al.*, From biomass to high performance solar–thermal and electric–thermal energy conversion and storage materials, *J. Mater. Chem. A*, 2014, **2**(21), 7759–7765.
5 S. Gao, *et al.*, Carbon foam/reduced graphene oxide/paraffin composite phase change material for electromagnetic interference shielding and thermal management, *J. Energy Storage*, 2023, **58**, 106355.
6 W. Cui, *et al.*, Thermal performance of modified melamine foam/graphene/paraffin wax composite phase change materials for solar-thermal energy conversion and storage, *J. Cleaner Prod.*, 2022, **367**, 133031.
7 J. Wang, *et al.*, Highly flexible phase-change film with solar thermal storage and sensitive motion detection for wearable thermal management, *Chem. Eng. J.*, 2023, **466**, 143334.
8 Z. Said, *et al.*, Sustainable Thermal Solutions: Enhancing Heat Transfer with Turbulators and Nanofluids, *Adv. Energy Sustainability Res.*, 2025, 2400335.
9 X. Sun, *et al.*, Enhanced thermal energy storage of a paraffin-based phase change material (PCM) using nano carbons, *Appl. Therm. Eng.*, 2020, **181**, 115992.
10 M. Maleki, *et al.*, Development of graphitic domains in carbon foams for high efficient electro/photo-to-thermal energy conversion phase change composites, *Chem. Eng. J.*, 2019, **362**, 469–481.
11 R. Gulfam, P. Zhang and Z. Meng, Advanced thermal systems driven by paraffin-based phase change materials – A review, *Appl. Energy*, 2019, **238**, 582–611.
12 Z. Wang, *et al.*, Preparation and thermal properties of shape-stabilized composite phase change materials based on paraffin wax and carbon foam, *Polymer*, 2021, **237**, 124361.
13 R. D. McKerracher, *et al.*, Advances in Prevention of Thermal Runaway in Lithium-Ion Batteries, *Adv. Energy Sustainability Res.*, 2021, **2**(5), 2000059.
14 Z. Hu, *et al.*, MoS2-decorated carbonized melamine foam/reduced graphene oxide network for constructing polyethylene-glycol-based multifunctional phase change materials toward multiple energy harvesting and microwave absorbing applications, *Chem. Eng. J.*, 2023, **461**, 141923.
15 Y. Lu, *et al.*, Novel smart textile with phase change materials encapsulated core-sheath structure fabricated by coaxial electrospinning, *Chem. Eng. J.*, 2019, **355**, 532–539.
16 F. Lin, *et al.*, Grid structure phase change composites with effective solar/electro-thermal conversion for multifunctional thermal application, *Carbon*, 2023, **201**, 1001–1010.
17 P. Tao, *et al.*, Magnetically-accelerated large-capacity solar-thermal energy storage within high-temperature phase-change materials, *Energy Environ. Sci.*, 2019, **12**(5), 1613–1621.
18 Y. Chen, *et al.*, Enhanced light-to-thermal conversion performance of self-assembly carbon nanotube/graphene-interconnected phase change materials for thermal-electric device, *J. Energy Storage*, 2023, **72**, 108387.
19 K. Wang, *et al.*, A Review on Microencapsulated Phase-Change Materials: Preparation, Photothermal Conversion Performance, Energy Storage, and Application, *Sol. RRL*, 2023, **7**(22), 2300447.
20 M. M. Umair, *et al.*, Novel strategies and supporting materials applied to shape-stabilize organic phase change materials for thermal energy storage–A review, *Appl. Energy*, 2019, **235**, 846–873.

21 M. Ebrahimi, *et al.*, In-situ synthesis of nanoporous nickel/carbon composite foam to encapsulate the phase change materials for energy management, *J. Energy Storage*, 2024, **102**, 113915.
22 Z. A. Qureshi, H. M. Ali and S. Khushnood, Recent advances on thermal conductivity enhancement of phase change materials for energy storage system: A review, *Int. J. Heat Mass Transfer*, 2018, **127**, 838–856.
23 P. Jana, *et al.*, Thermal conductivity improvement of composite carbon foams based on tannin-based disordered carbon matrix and graphite fillers, *Mater. Des.*, 2015, **83**, 635–643.
24 P. Jana, V. Fierro and A. Celzard, Sucrose-based carbon foams with enhanced thermal conductivity, *Ind. Crops Prod.*, 2016, **89**, 498–506.
25 X. Su, *et al.*, A Unique Strategy for Polyethylene Glycol/Hybrid Carbon Foam Phase Change Materials: Morphologies, Thermal Properties, and Energy Storage Behavior, *Materials*, 2018, **11**, 2011.
26 J. Yang, *et al.*, Hybrid graphene aerogels/phase change material composites: Thermal conductivity, shape-stabilization and light-to-thermal energy storage, *Carbon*, 2016, **100**, 693–702.
27 K. Zhou, *et al.*, Biomass porous carbon/polyethylene glycol shape-stable phase change composites for multi-source driven thermal energy conversion and storage, *Adv. Compos. Hybrid Mater.*, 2023, 6.
28 X. Luo, *et al.*, Modified phase change materials used for thermal management of a novel solar thermoelectric generator, *Energy Convers. Manage.*, 2020, **208**, 112459.
29 S. Song, *et al.*, Carbon aerogel based composite phase change material derived from kapok fiber: Exceptional microwave absorbility and efficient solar/magnetic to thermal energy storage performance, *Composites, Part B*, 2021, **226**, 109330.
30 T. Xiao, *et al.*, In Situ Encapsulation of Phase-Change Thermal-Storage Material using 3D Polymer-Aided Cross-Linked Porous Carbon, *Adv. Energy Sustainability Res.*, 2023, **4**(3), 2200164.
31 G. Li, *et al.*, From anisotropic graphene aerogels to electron- and photo-driven phase change composites, *J. Mater. Chem. A*, 2016, **4**(43), 17042–17049.
32 G. Qi, *et al.*, Hierarchical graphene foam-based phase change materials with enhanced thermal conductivity and shape stability for efficient solar-to-thermal energy conversion and storage, *Nano Res.*, 2017, **10**, 802–813.
33 R. Fan, *et al.*, A scalable phase change material-based system enhanced by multi-walled carbon nanotubes and fins for efficient solar water heating applications, *J. Energy Storage*, 2023, **72**, 108791.
34 C. Yu, *et al.*, Enhancement of Structural Stability of Graphene Aerogel for Thermal Energy Harvesting, *ACS Appl. Energy Mater.*, 2021, **4**(10), 11666–11674.
35 C. Selvam, *et al.*, Enhanced thermal performance of a thermoelectric generator with phase change materials, *Int. Commun. Heat Mass Transfer*, 2020, **114**, 104561.
36 F. Rajaee, *et al.*, Experimental analysis of a photovoltaic/thermoelectric generator using cobalt oxide nanofluid and phase change material heat sink, *Energy Convers. Manage.*, 2020, **212**, 112780.
37 C. Yu and Y. S. Song, Modification of Graphene Aerogel Embedded Form-Stable Phase Change Materials for High Energy Harvesting Efficiency, *Macromol. Res.*, 2022, **30**(3), 198–204.
38 C. Yu and Y. S. Song, Advanced internal porous skeleton supported phase change materials for thermo-electric energy conversion applications, *J. Polym. Res.*, 2022, **29**(3), 79.
39 A. Mohseni Ahangar, *et al.*, Highly graphitized carbon foam to construct phase change materials composites for multiple solar−thermal energy conversion, *Sol. Energy Mater. Sol. Cells*, 2024, **277**, 113084.
40 Y. Wu, *et al.*, High-Efficiency Photo-Thermo-Electric System with Waste Heat Utilization and Energy Storage, *ACS Appl. Mater. Interfaces*, 2022, **14**(35), 40437–40446.
41 P. Cheng and D. Wang, Easily Repairable and High-Performance Carbon Nanostructure Absorber for Solar Photothermoelectric Conversion and Photothermal Water Evaporation, *ACS Appl. Mater. Interfaces*, 2023, **15**(6), 8761–8769.
42 M. Maleki, *et al.*, Electro-driven carbon foam/PCMs nanocomposites for sustainable energy management, *J. Energy Storage*, 2023, **67**, 107599.
43 Y. Zhang, *et al.*, Phase change materials for electron-triggered energy conversion and storage: a review, *J. Mater. Chem. A*, 2019, **7**(39), 22218–22228.
44 X. Guo, *et al.*, Electrothermal conversion phase change composites: the case of polyethylene glycol infiltrated graphene oxide/carbon nanotube networks, *Ind. Eng. Chem. Res.*, 2018, **57**(46), 15697–15702.
45 M. Inagaki and F. Kang, *Materials Science and Engineering of Carbon: Fundamentals*, 2nd edn, 2014, pp. 1–539.
46 D. Wang, *et al.*, Lightweight waterproof magnetic carbon foam for multifunctional electromagnetic wave absorbing material, *Carbon*, 2023, **202**, 464–474.
47 K. Sun, *et al.*, The design of phase change materials with carbon aerogel composites for multi-responsive thermal energy capture and storage, *J. Mater. Chem. A*, 2021, **9**(2), 1213–1220.
48 X.-H. Li, *et al.*, Thermally annealed anisotropic graphene aerogels and their electrically conductive epoxy composites with excellent electromagnetic interference shielding efficiencies, *ACS Appl. Mater. Interfaces*, 2016, **8**(48), 33230–33239.
49 J. Gao, *et al.*, Engineering Electronic Transfer Dynamics and Ion Adsorption Capability in Dual-Doped Carbon for High-Energy Potassium Ion Hybrid Capacitors, *ACS Nano*, 2022, **16**(4), 6255–6265.
50 Z. Song, *et al.*, High-energy flexible solid-state supercapacitors based on O, N, S-tridoped carbon electrodes and a 3.5 V gel-type electrolyte, *Chem. Eng. J.*, 2019, **372**, 1216–1225.
51 Y. Lu, *et al.*, Hypercrosslinked polymers enabled micropore-dominant N, S Co-Doped porous carbon for ultrafast

electron/ion transport supercapacitors, *Nano Energy*, 2019, **65**, 103993.
52 H. Banna Motejadded Emrooz, M. Maleki and A. Rahmani, Azolla-derived hierarchical nanoporous carbons: From environmental concerns to industrial opportunities, *J. Taiwan Inst. Chem. Eng.*, 2018, **91**, 281–290.
53 N. Ukrainczyk, S. Kurajica and J. Šipušić, Thermophysical comparison of five commercial paraffin waxes as latent heat storage materials, *Chem. Biochem. Eng. Q.*, 2010, **24**(2), 129–137.
54 M. Maleki, *et al.*, Photo-thermal conversion structure by infiltration of paraffin in three dimensionally interconnected porous polystyrene-carbon nanotubes (PS-CNT) polyHIPE foam, *Sol. Energy Mater. Sol. Cells*, 2019, **191**, 266–274.
55 M. Mehrali, *et al.*, Shape-stabilized phase change materials with high thermal conductivity based on paraffin/graphene oxide composite, *Energy Convers. Manage.*, 2013, **67**, 275–282.
56 J. Wang, *et al.*, Synthesis of ''graphene-like'' mesoporous carbons for shape-stabilized phase change materials with high loading capacity and improved latent heat, *J. Mater. Chem. A*, 2017, **5**(46), 24321–24328.
57 K. Yuan, *et al.*, Engineering the thermal conductivity of functional phase-change materials for heat energy conversion, storage, and utilization, *Adv. Funct. Mater.*, 2020, **30**(8), 1904228.
58 R. Wu, *et al.*, A novel three-dimensional network-based stearic acid/graphitized carbon foam composite as high-performance shape-stabilized phase change material for thermal energy storage, *Composites, Part B*, 2021, **225**, 109318.
59 M. Li and B. Mu, Effect of different dimensional carbon materials on the properties and application of phase change materials: A review, *Appl. Energy*, 2019, **242**, 695–715.
60 P. Wilson, S. Vijayan and K. Prabhakaran, Thermally Conducting Microcellular Carbon Foams as a Superior Host for Wax-Based Phase Change Materials, *Adv. Eng. Mater.*, 2019, **21**(4), 1801139.
61 H. Liu, X. Wang and D. Wu, Innovative design of microencapsulated phase change materials for thermal energy storage and versatile applications: a review, *Sustainable Energy Fuels*, 2019, **3**(5), 1091–1149.
62 M. Karthik, A. Faik and B. D'Aguanno, Graphite foam as interpenetrating matrices for phase change paraffin wax: A candidate composite for low temperature thermal energy storage, *Sol. Energy Mater. Sol. Cells*, 2017, **172**, 324–334.
63 H. Yang, *et al.*, Modified melamine foam-based flexible phase change composites: Enhanced photothermal conversion and shape memory properties, *ACS Appl. Polym. Mater.*, 2021, **3**(7), 3321–3333.
64 W. Wang, *et al.*, Ultralight and flexible carbon foam-based phase change composites with high latent-heat capacity and photothermal conversion capability, *ACS Appl. Mater. Interfaces*, 2019, **11**(35), 31997–32007.
65 A. R. Akhiani, *et al.*, Highly hydrophobic silanized melamine foam for facile and uniform assembly of graphene nanoplatelet towards efficient light-to-thermal energy storage, *Mater. Today Energy*, 2022, **28**, 101077.
66 L. Zhang, *et al.*, Solar-thermal conversion and thermal energy storage of graphene foam-based composites, *Nanoscale*, 2016, **8**(30), 14600–14607.
67 J. Yang, *et al.*, Hybridizing graphene aerogel into three-dimensional graphene foam for high-performance composite phase change materials, *Energy Storage Mater.*, 2018, 13.
68 C. Wang, *et al.*, Biomass carbon aerogels based shape-stable phase change composites with high light-to-thermal efficiency for energy storage, *Renewable Energy*, 2020, **153**, 182–192.
69 H. He, *et al.*, A multifunctional carbon-base phase change composite inspired by ''fruit growth'', *Carbon*, 2023, **205**, 499–509.
70 L. Chen, *et al.*, Cost-effective, scalable fabrication of self-floating xerogel foam for simultaneous photothermal water evaporation and thermoelectric power generation, *Chem. Eng. J.*, 2023, **454**, 140383.
71 B. Aljafari, *et al.*, Organic/carbon and organic/carbon-metal composite phase change material for thermoelectric generator: Experimental evaluation, *J. Energy Storage*, 2024, **78**, 110082.
72 T. Shi, H. Liu and X. Wang, Unidirectionally Structured Magnetic Phase-Change Composite Based on Carbonized Polyimide/Kevlar Nanofiber Complex Aerogel for Boosting Solar-Thermo-Electric Energy Conversion, *ACS Appl. Mater. Interfaces*, 2024, **16**(8), 10180–10195.
73 Z. Liu, *et al.*, Tailoring Carbon Nanotube Density for Modulating Electro-to-Heat Conversion in Phase Change Composites, *Nano Lett.*, 2013, **13**(9), 4028–4035.
74 W. Wu, *et al.*, A functional form-stable phase change composite with high efficiency electro-to-thermal energy conversion, *Appl. Energy*, 2017, **190**, 474–480.
75 X. Chen, *et al.*, Phase change materials for electro-thermal conversion and storage: from fundamental understanding to engineering design, *iScience*, 2020, **23**(6), 101208.
76 F. Xue, *et al.*, Melamine foam-templated graphene nanoplatelet framework toward phase change materials with multiple energy conversion abilities, *Chem. Eng. J.*, 2019, **365**, 20–29.
77 M. M. Umair, *et al.*, A novel flexible phase change composite with electro-driven shape memory, energy conversion/storage and motion sensing properties, *J. Mater. Chem. A*, 2019, **7**(46), 26385–26392.